Chemical Science

ROYAL SOCIETY OF CHEMISTRY

EDGE ARTICLE

View Article Online
View Journal | View Issue

Cite this: *Chem. Sci.*, 2025, **16**, 20959

All publication charges for this article have been paid for by the Royal Society of Chemistry

Stabilizing the oxygen anionic redox chemistry using a Li-deficient and Li-rich biphasic structure for high-energy Li-ion batteries

Feng Li, †[a] Jiacheng Li,†[a] Peiyu Hou, *[a] Zezhou Lin, [b] Mohan Dong,[a] Lin-Hui Wang,*[c] Hongzhou Zhang *[d] and Xijin Xu *[a]

Li-rich layered oxides (LLOs) with a large specific capacity of ~300 mAh g^{-1} show promise for developing high-energy Li-ion batteries (LIBs). However, the thermodynamic instability of the oxygen-anionic redox couple leads to lattice oxygen loss and structural transformation, resulting in a rapid decline in voltage and capacity. In this work, we rationally engineer Li-deficient phase formation in LLOs to stabilize oxygen-anionic redox chemistry and improve structural stability. The Li-deficient and Li-rich biphasic intergrowth composite is synthesized *via* ion exchange from the P3/O3 intermediate mixed-phase oxides. It is found that the incorporation of the Li-deficient phase makes the movement of the O 2p non-bonding energy band toward lower energy, which further alleviates the lattice oxygen release and stabilizes the oxygen-anionic redox chemistry upon Li^+ de-intercalation. Consequently, the cycling stability is significantly enhanced in the biphasic LLOs, retaining superior capacity/voltage retention of ~86%/88% after 400 cycles with a low capacity decay rate of 0.034% and voltage decline of 1.06 mV per cycle. The biphasic design offers a simple and feasible strategy for regulating the oxygen-anionic redox chemistry and boosting the structural stability of high-capacity LLOs.

Received 24th June 2025
Accepted 5th September 2025

DOI: 10.1039/d5sc04623h

rsc.li/chemical-science

1 Introduction

The state-of-the-art Li-ion battery (LIB) with the advantages of high energy/power density and long lifespan has shown promise for promoting the applications of electric vehicles (EVs) and renewable clean energy.[1] The performance and cost of LIBs highly depend on the cathode materials and thereby developing high-capacity/voltage and inexpensive cathodes becomes extremely urgent.[2] Low-cost Mn-based materials have attracted much attention due to the earth-abundant sources.[3] In particular, Mn-based LLOs deliver a high specific capacity of around 300 mAh g^{-1} owing to the new reaction mechanism involving anionic and cationic coexisting redox.[4,5] Thus Mn-based LLOs as desired cathode materials have shown potential for the development of high-energy and low-cost LIBs.[4,6,7]

Apart from the traditional transition-metal (TM) cationic redox that occurs in layered $LiTMO_2$, the oxygen-anionic redox plays a vital role in the improvement of the reversible capacity of LLOs.[8,9] But the thermodynamic instability of the oxygen-anionic redox gives rise to some great challenges, especially voltage/capacity decline, voltage hysteresis, inferior high-rate capability, and poor initial coulombic efficiency (ICE). Bruce *et al.* revealed that voltage hysteresis was related to the formation of oxygen molecules trapped in defects within the bulk LLOs.[10] Tarascon *et al.* found that voltage hysteresis was induced by the slow kinetics and progressive overoxidation of the oxygen-anionic redox.[11] At the deeply delithiated state of LLOs, the overoxidation and enhanced mobility of O^{n-} ($n < 2$) anions cause the lattice oxygen release and the generation of oxygen vacancies thereby resulting in the TM movement into Li 3a vacancies, and further triggering the structural evolutions from layered to the spinel/rock-salt structure.[12,13] The structural changes are usually accompanied by a voltage/capacity decline in these LLOs. The persistent accumulation of the cathode electrolyte interphase (CEI) generated by the side reactions between overoxidation anions and organic electrolyte decreases the interfacial charge transfer during redox reactions.[14,15]

The strategies of surface coating, foreign-ion doping, and structural optimization have been broadly utilized to mitigate the performance degradation in LLOs. Guo *et al.* confirmed that $Li_4Mn_5O_{12}$ as a new surface coating layer suppressed the oxygen loss and retained the stability of the oxygen-anionic redox.[16] Ma *et al.* found that the concentration-gradient W^{6+} doping alleviated structural deterioration and improved the stability of the

[a]*School of Physics and Technology, University of Jinan, Jinan, Shandong Province, 250022, China. E-mail: sps_houpy@ujn.edu.cn; sps_xuxj@ujn.edu.cn*

[b]*Department of Applied Physics and Research Institute for Smart Energy, The Hong Kong Polytechnic University, Hong Kong, China*

[c]*College of Information Science and Engineering, Shandong Agricultural University, Tai'an, Shandong Province, 271018, China. E-mail: linhuiwang@sdau.edu.cn*

[d]*Tianjin Key Laboratory for Photoelectric Materials and Devices, School of Materials Science and Engineering, Tianjin University of Technology, Tianjin, 300384, China. E-mail: zhanghongzhou@mail.nankai.edu.cn*

† F. L. and J. L. contributed equally to this work.

electrode/electrolyte interface.[17] Chen *et al.* revealed that Li/Ni disordering and Li 3a vacancies suppressed the formation of the O–O dimer and thereby enhanced the stability of the oxygen-anionic redox.[18] Recently, Xia *et al.* proposed a new O2-type LLO $Li_{1.25}Co_{0.25}Mn_{0.50}O_2$ *via* an ion exchange reaction.[19] The voltage stability was significantly boosted by generating the single-layer Li_2MnO_3 superlattice. Wang *et al.* found that the formation of the fluorinated solid electrolyte interphase (SEI) in all-fluorinated electrolytes could stabilize the O2-type LLO.[20] Kang *et al.* demonstrated that the O2-type structure restricted the movement of TM into the Li vacancies in high voltage regions, and thereby remarkably reduced their voltage decline.[21]

Recently, the introduction of Li vacancies in Mn-based oxide cathodes has been shown to be very promising in stabilizing their structural stability.[22,23] In this work, Li-rich and Li-deficient biphasic intergrowth LLOs are rationally designed to stabilize their oxygen-anionic redox chemistry and improve their electrochemical behavior. Considering the phase transformation from the Na-deficient P3 phase to Li-deficient O3 phase in the binary molten salt system of $LiNO_3$/LiCl,[24] the Li-rich and Li-deficient biphasic LLOs are prepared by ion exchange from the P3/O3-type intermediate mixed-phase oxides, as depicted in Scheme 1. The incorporation of a Li-deficient structure into the high-capacity LLOs is expected to suppress the lattice oxygen loss and further stabilize the oxygen-anionic redox chemistry. Consequently, the voltage stability, reversible capacity, and ICE are significantly improved for these proposed biphasic intergrowth LLOs. These achievements demonstrate the feasibility of tuning oxygen-anionic chemistry and improving the structural stability of LLOs by the introduction of the Li-deficient phase.

2 Results and discussion

The target $[Ni_{0.3}Co_{0.1}Mn_{0.6}](OH)_2$ precursors are first synthesized *via* a co-precipitation reaction. The morphology of as-prepared precursor particles is investigated by SEM, as shown in Fig. S1. It exhibits near-spherical secondary particles with a particle size of 10–15 μm assembled from numerous nanosheet primary grains. The formation of spherical precursors mainly involves the dissolution–recrystallization mechanism.[25] Specifically, the primordially generated small primary grains are consumed and further grow on the formed particles to minimize the overall surface free energy. First, the ionized TM^{2+} ($TM = Ni_{0.3}Co_{0.1}Mn_{0.6}$) ions react with NH_3 ligands and generate a stable complex $[TM(NH_3)_n]^{2+}$ to decrease the free concentration of TM^{2+}. This complex reacts with OH^- and produces the primary $TM(OH)_2$ grains. Second, these tiny $TM(OH)_2$ grains are consumed and further grow on the formed particles *via* the dissolution–recrystallization mechanism. The actual chemical composition of the as-prepared precursors is analyzed by inductively coupled plasma optical emission spectrometry (ICP-OES), as shown in Table S1. ICP-OES results show that the molar ratio of Ni/Co/Mn is 0.298/0.099/0.603, indicating the chemical formula of $[Ni_{0.298}Co_{0.099}Mn_{0.603}](OH)_2$ for the precursors, which matches the designed component. The precursors mixed with stoichiometric Li_2CO_3 and Na_2CO_3 (Na/TM = 0.4 and Li/TM = 1.0) were calcined at 800 °C to prepare the P3/O3 biphasic composite as an intermediate phase. Fig. S2 shows the SEM and XRD of the formed P3/O3 biphasic composite. The near-spherical particles of the P3/O3 biphasic composite are well maintained after solid-state reactions between precursors and Li/Na sources. However, the primary grains show some changes and grow up obviously in this P3/O3 biphasic composite compared with that of hydroxide precursors (Fig. S1). The XRD pattern exhibits diffraction lines that can be ascribed to the O3-phase and P3-phase with the same space group of $R\bar{3}m$, confirming the formation of a P3/O3 biphasic structure by tuning the molar ratios of Na/TM and Li/TM. Due to the strong electrostatic repulsion effect between sodium ions, adjacent prismatic sodium sites cannot be occupied simultaneously within the P3-type crystal structure. The sodium stoichiometry usually ranges from 0.5 to 0.8, and the sodium-deficient nature is generated in the P3-type oxides.[26]

The Na-deficient P3 phase will transform into the Li-deficient O3 phase during Na/Li ion exchange reactions.[24,27] Namely, the molar ratio of P3 and O3 phases will determine the final O3′/O3 ratio in the hybrid material. Considering the Na-containing P3 structure and Li-containing O3 structure, the Na and Li stoichiometries (Na/TM and Li/TM) during solid-state reactions will affect the molar ratio of P3 and O3 phases and further determine the O3′/O3 ratio in the BI-LLOs. Therefore,

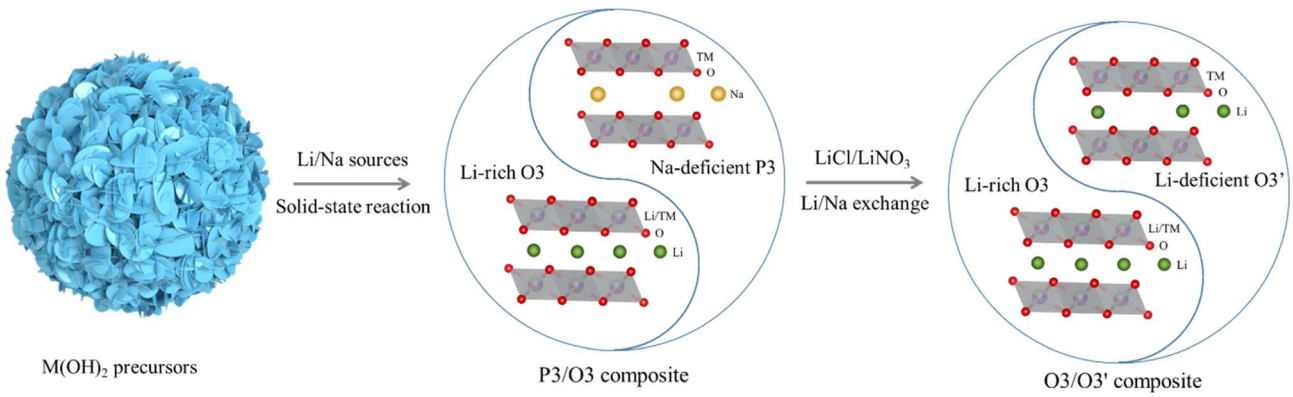

Scheme 1 Scheme of synthesis of Li-deficient and Li-rich biphasic intergrowth LLOs based on solid-state and ion-exchange reactions.

the molar ratio of O3′ and O3 phases within the designed BI-LLOs can be regulated by tuning Na and Li stoichiometries during the first-step solid-state reaction. The Li-rich and Li-deficient biphasic intergrowth Li-rich layered oxides (BI-LLOs) are prepared from the P3/O3 intermediate mixed-phase in the binary molten salt system. SEM, HRTEM, XRD, and Rietveld refinements of BI-LLOs are shown in Fig. 1. The BI-LLOs still show near-spherical polycrystalline particles assembled from nanosheet grains, as seen in Fig. 1(a). The BI-LLOs have similar morphology to the P3/O3 composite, indicating that the low-temperature (L-T) ion-exchange reaction does not break the particle integrity. The EDS elemental mapping in Fig. S3 indicates the monodispersity of Mn/Ni/Co/O elements in the BI-LLOs. The SEM image of the single-phase Li-rich layered oxides (SP-LLOs) in Fig. S4 also shows near-spherical secondary particles. XRD patterns of the BI-LLOs and the enlarged region of 35–50° are shown in Fig. 1(c) and (d), respectively. The obvious split of (015) and (107) diffraction peaks is found for the BI-LLOs while the SP-LLOs only show a single peak without peak split (Fig. S5). The diffraction lines of BI-LLOs can be well indexed to the layered phase of the Li-rich structure and Li-deficient structure, which confirms the formation of biphasic intergrowth. HRTEM and inverse FFT images in region 1 (R1) of BI-LLOs show a series of fringe spacing with a *d*-spacing of ~0.2 nm in Fig. 1(b) and S6, corresponding to the (104) crystal plane of layered $LiTMO_2$. The inverse FFT image in region 2 (R2) likely shows the interference fringe with a *d*-spacing of ~0.47 nm, corresponding to the (003) crystal plane. The phase properties of both LLOs are studied by XRD and Rietveld refinement in Fig. 1(e) and S7. XRD patterns of BI-LLOs and SP-LLOs can be indexed to an α-$NaFeO_2$-type layered phase. The calculated crystal parameters by Rietveld refinement for both LLOs are given in Tables S2–S4. The refinement results reveal that the fractions of the Li-rich phase and Li-deficient phase in the BI-LLOs are 77% and 23%, respectively. And the Li-rich phase within BI-LLOs has a lattice parameter of c = 14.2853 Å, which is very similar to that of SP-LLOs (c = 14.2834 Å), indicating the very limited sodium incorporation into the bulk structure of BI-LLOs. Furthermore, Rietveld refinement reveals that the SP-LLOs possess only the Li-rich layered single phase. ICP-OES data show that the molar ratio of Li/Ni/Co/Mn is 1.159/0.251/0.083/0.505 and 1.163/0.252/0.083/0.502 for BI-LLOs and SP-LLOs, respectively, which indicates the chemical formulas of $Li_{1.159}[Ni_{0.251}Co_{0.083}Mn_{0.505}]O_2$ and $Li_{1.163}[Ni_{0.252}Co_{0.083}Mn_{0.502}]O_2$. These results confirm the feasibility of transformation from the Na-deficient P3-phase into the Li-deficient O3-phase oxide *via* ion exchange and preparation of Li-rich and Li-deficient BI-LLOs from the P3/O3 intermediate composite.

The electrochemical performance of BI-LLOs and SP-LLOs is measured, as shown in Fig. 2. The SP-LLOs only deliver a discharge capacity of 270.2 mAh g^{-1} at 0.1C with a low ICE of 76.2%. At the same charge–discharge rate, the BI-LLOs show a higher available capacity of 296.5 mAh g^{-1} with an improved ICE of 87.8% in Fig. 2(a). As for the SP-LLOs, the lattice oxygen loss occurs in the initial charging process and thereby results in structural reconstruction.[12,13] As a result, the extracted Li^+ ions

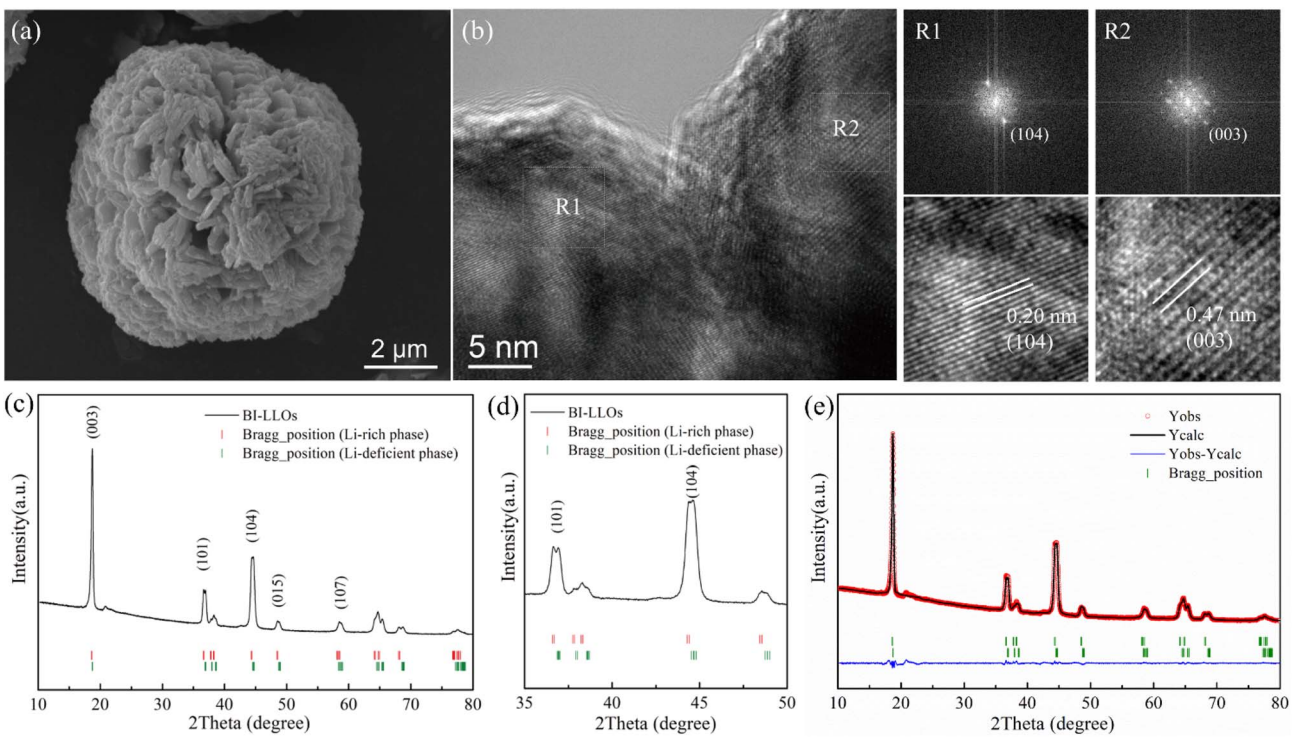

Fig. 1 (a) SEM image, (b) HRTEM image and (inverse) FFT images, and (c–e) XRD and Rietveld refinements of Li-rich and Li-deficient BI-LLOs. The refinement is based on the Li-rich $Li_{1.2}[Ni_{0.3}Co_{0.1}Mn_{0.6}]_{0.8}O_2$ hexagonal ($R\bar{3}m$) phase and Li-deficient $Li_{0.85}[Ni_{0.3}Co_{0.1}Mn_{0.6}]O_2$ hexagonal ($R\bar{3}m$) phase.

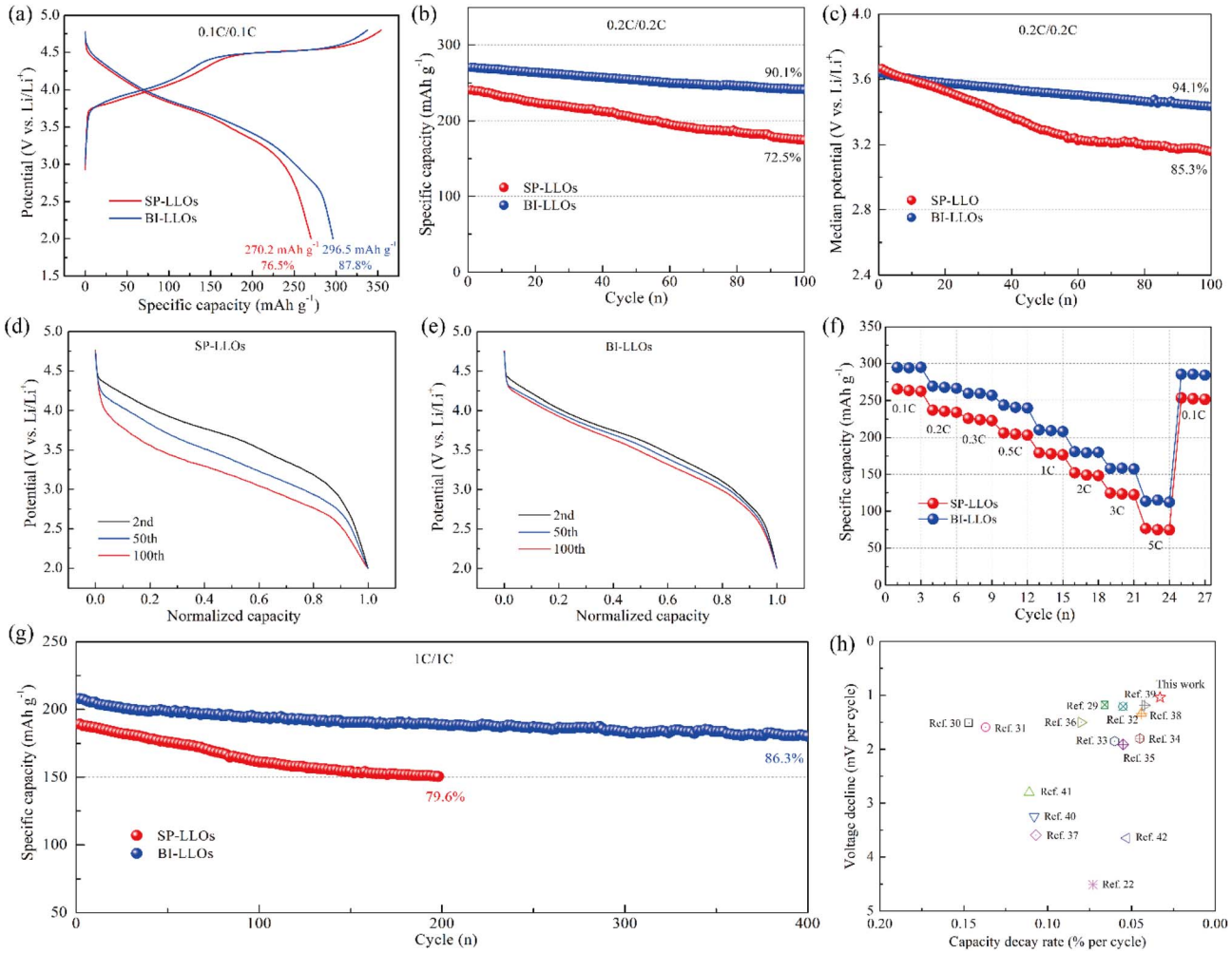

Fig. 2 (a) The first charge–discharge curves, (b and c) cycling stability of capacity and median voltage, (d and e) the changes of normalized discharge profile upon repeated cycles, (f) rate capability and (g) long-term cycling performance of BI-LLOs and SP-LLOs. (h) Comparison of capacity and voltage of recently reported biphasic LLOs and the present study's Li-deficient and Li-rich biphasic LLOs.

cannot be completely inserted into the bulk structure in the following discharging process, corresponding to a low ICE. The BI-LLOs possess the Li-deficient and Li-rich biphasic intergrowth behavior, while the Li-deficient structure has some Li vacancies in the pristine state. During the initial discharging process, Li^+ ions can be inserted into these vacancies accompanied by reduction of Mn ions, which improves the ICE and available capacity. The BI-LLOs exhibit a weak discharge platform below 3.0 V in the initial discharge process, which is probably ascribed to the activation of the redox couple of $Mn^{3+/4+}$. A previous report has demonstrated that the melting chemical reaction during Na/Li ion exchange induces the valence reduction of Mn ions and further activates the $Mn^{3+/4+}$ redox couple.[28] The activation of the redox couple of $Mn^{3+/4+}$ in the BI-LLOs significantly boosts the reversible capacity and ICE, but this low-voltage platform decreases the median potential compared with that of SP-LLOs.

The cycling stability of LLOs is remarkably enhanced by building the biphasic intergrowth composite. The BI-LLOs reveal a better capacity retention of 90.1% within 100 charge–discharge cycles at 0.2C than that of 72.5% of SP-LLOs as shown in Fig. 2(b). The BI-LLOs also show a higher charge–discharge coulombic efficiency than that of SP-LLOs, as shown in Fig. S8. Besides, the BI-LLOs also possess superior potential stability during repeated cycling, giving a high median potential of 3.435 V as shown in Fig. 2(c). But the SP-LLOs show a rapid decline in discharge potential, retaining a low median potential of 3.157 V after the same number of cycles. The improved stability of potential and capacity further gives rise to the enhanced stability of energy density for BI-LLOs, as shown in Fig. S9. The evolutions of the charge–discharge curves from the 2nd to 100th cycle are shown in Fig. S10. The SP-LLOs reveal a continuously increasing charge platform and decreasing discharge platform as the number of cycles increases, indicating the incremental polarization. Interestingly, the BI-LLOs present weak polarization within the repeated charge–discharge cycles. The normalized discharge capacities of SP-LLOs and BI-LLOs are shown in Fig. 2(d) and (e), respectively, in which the profiles of SP-LLOs show a significantly lowered discharge platform, corresponding to the voltage decline.

Fig. 2(f) shows the rate properties of BI-LLOs and SP-LLOs. The BI-LLOs show the available capacities of 294, 269, 260, 241, 210, 180, 158, and 114 mAh g^{-1} at 0.1C, 0.2C, 0.3C, 0.5C, 1C, 2C, 3C to 5C, respectively. As the rate recovers from a high rate of 5C to the initial 0.1C, the high specific capacity of 285 mAh g^{-1} is obtained for BI-LLOs, indicating the superior redox reversibility. The SP-LLOs deliver the specific capacities of 265, 236, 225, 205, 180, 150, 124, and 75 mAh g^{-1} at the same rates, respectively. The BI-LLOs deliver higher available capacities, especially at high rates of above 1C, suggesting a better high-rate capability. The charge–discharge profiles (Fig. S11) exhibit anabatic electrochemical polarization when the charge–discharge rate exceeds 2C. The long-term cycling performance of both LLOs is tested at 1C, as shown in Fig. 2(g) and S12. The SP-LLOs exhibit a fast capacity/voltage decline and a capacity retention of 79.6% and retain a low median voltage of ~2.85 V only after 200 charge–discharge cycles. The BI-LLOs show an outstanding capacity retention of 86.3% and retain a high median voltage of ~3.05 V even after 400 cycles, suggesting the improved thermodynamic stability by rational design of the Li-deficient and Li-rich biphasic structure. Overall, we demonstrate that the rational design of the Li-rich and Li-deficient biphasic structure remarkably improves the discharge specific capacity, cycling stability, high-rate capability, and ICE. A comparison of capacity and voltage of recently reported biphasic LLOs and the present study's Li-deficient and Li-rich biphasic LLOs is shown in Fig. 2(h) and Table S5. The BI-LLOs in our study show a lower capacity decay rate of 0.034% and a weaker voltage decline of 1.06 mV per cycle than the recent reports with biphasic structures.[22,29–42]

In the initial charge–discharge cycle, a long charge platform at ~4.6 V ascribed to oxidation of lattice oxygen is detected in these reported LLOs, which involves irreversible oxygen activation and O_2 loss.[43,44] The O_2 loss from the bulk structure accompanies structural reconfiguration and phase transition, which further results in the low ICE and rapid capacity/voltage decline.[6,7] An *operando* differential electrochemical mass spectrometer (DEMS) is employed to evaluate the evolutions of oxygen redox behavior of both LLOs as shown in Fig. 3(a) and (b). The peak value of the O_2 loss rate of SP-LLOs occurs at about 4.7 V, reaching as high as 2.67 μmol g^{-1} h^{-1} in the initial cycle, much higher than that of the BI-LLOs (0.98 μmol g^{-1} h^{-1}). The decreased O_2 loss in the first cycle leads to the alleviative reconfiguration of the crystal structure and thereby gives rise to a high ICE (~88%) for BI-LLOs. In addition, the O_2 loss rate of BI-LLOs decreases drastically in the second cycle, approaching zero. Nevertheless, SP-LLOs still show a maximal O_2 loss rate of 1.19 μmol g^{-1} h^{-1} in the second cycle. DEMS analysis confirms

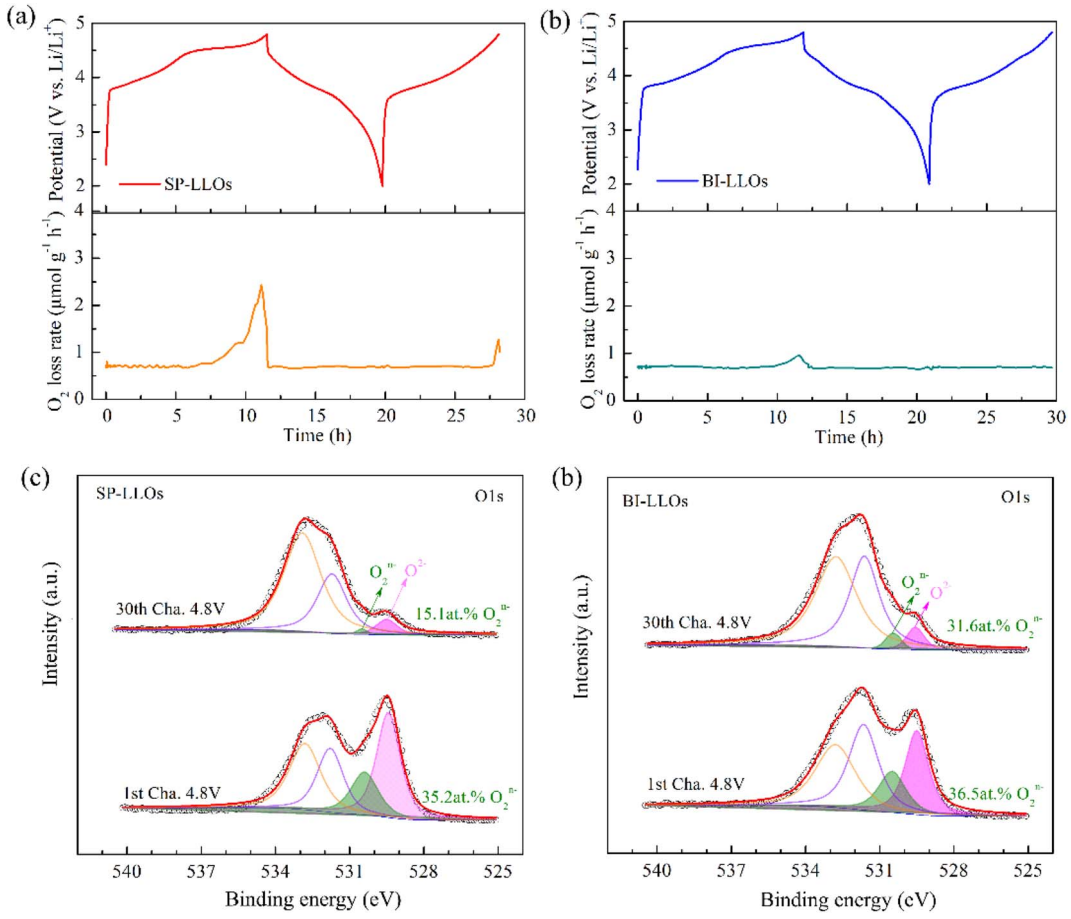

Fig. 3 (a and b) *Operando* DEMS analysis during the initial charge–discharge of SP-LLOs and BI-LLOs at 0.1C, respectively. (c and d) XPS spectra of O 1s measured within the 1st and 30th cycle at the highly delithiated state of 4.8 V.

that the proposed biphasic structure effectively alleviates the intractable problem of irreversible O_2 loss, suggesting the improved reversible chemistry of oxygen-anionic redox chemistry during cycling.[45,46]

The reversible changes of the anionic $O^{2-}/(O_2)^{n-}$ redox couple are further measured by X-ray photoelectron spectroscopy (XPS). The XPS spectra of O 1s measured within the 1st and 30th cycle at the highly delithiated state of 4.8 V are shown in Fig. 3(c) and (d). It is found that the O 1s spectra are composed of three kinds of oxygen species, *i.e.*, oxygen-containing CEI (BEs at ~531.8 and 533.1 eV), oxidized lattice $(O_2)^{n-}$ (BE at ~530.4 eV), and lattice O^{2-} (BE at ~529.4 eV).[47,48] We calculate the molar ratio of $(O_2)^{n-}$ on the basis of the area proportion of the given fitting peak at ~530.4 eV. For the SP-LLOs, the content of $(O_2)^{n-}$ decreases drastically from 35.2 at% (1st cycle) to 15.1 at% (30th cycle), suggesting the significantly decreased contribution and inferior stability of the oxygen-anionic redox. Interestingly, the BI-LLOs exhibit stable $(O_2)^{n-}$ content from 36.5 at% to 31.6 at% cycled from the 1st to 30th cycle, which demonstrates the stable oxygen-anionic redox contribution. The dQ/dV plots of both LLOs after varied charge–discharge cycles are shown in Fig. S13. For the SP-LLOs, the oxygen-anionic redox couple of $O^{2-}/(O_2)^{n-}$ and cation redox couples of $Ni^{2+/3+/4+}$ and $Co^{3+/4+}$ reduce remarkably while the $Mn^{3+/4+}$ redox couple increases during cycling. The BI-LLOs show the stable contributions of both anionic and cationic redox reactions upon repeated cycles. The XPS and dQ/dV results confirm more reversible changes of oxygen-anionic and TM-cationic valences in the BI-LLOs, which is probably ascribed to the reduced O_2 loss as confirmed by the above DEMS. Overall, the Li-deficient and Li-rich biphasic structure suppresses irreversible O_2 loss, boosts the reversibility of $O^{2-}/(O_2)^{n-}$, and further enables the stable oxygen-anionic and TM-cationic redox contributions.

As described above, apart from the traditional TM cationic redox occurring in $LiTMO_2$, the oxygen-anionic redox in Li_2MnO_3 plays a vital role in the improvement of the reversible capacity of LLOs. The structural nature of LLOs is a solid solution or a nanoscale composite of the Li_2MnO_3 phase and $LiTMO_2$ phase.[5] In the Li_2MnO_3 phase, one third of Mn ions in the TM sites are substituted by Li ions, leading to plenty of linear Li–O–Li configurations, where each O atom is coordinated by six Li/TM atoms. As a result, certain O 2p energy level orbitals are less hybridized with the TM d energy level orbitals. These oxygen anions in LLOs can be oxidized more easily when the cathode is charged to high voltages exceeding 4.5 V and further contribute to more reversible capacity in charge–discharge cycles.

To further illustrate the effect of incorporation of Li vacancies on oxygen-anionic redox chemistry of LLOs, density functional theory (DFT) calculations with a supercell of Li-deficient $Li_{50}[Ni_{15}Mn_{45}]O_{120}$ and Li-rich $Li_{60}[Li_{12}Ni_{12}Mn_{36}]O_{120}$ are performed. The covalent bonds between highly oxidized 3d TM and O 2p easily generate when charged above 4.5 V.[49] One O anion surrounded by six Li^+/Mn^{4+} cations tends to produce an O non-bonding state on the top of the O^{2-} band. Fig. 4(a) shows the density of states (DOS) of the O 2p orbitals and 3d TM orbitals for the Li-deficient and Li-rich structures. It is clear that the incorporation of Li vacancies significantly changes the DOS of LLOs. As for the Li-deficient structure, the O 2p non-bonding energy band moves towards lower energy, and the energy difference between Fermi level energy and O 2p is as high as 0.73 eV, indicating higher redox potential and better stability for oxygen-anionic redox chemistry.[50]

The excessive utilization of the oxygen anionic redox triggers local lattice oxygen mobility in the traditional LLOs. However, the oxygen mobility is accompanied by lattice oxygen release,

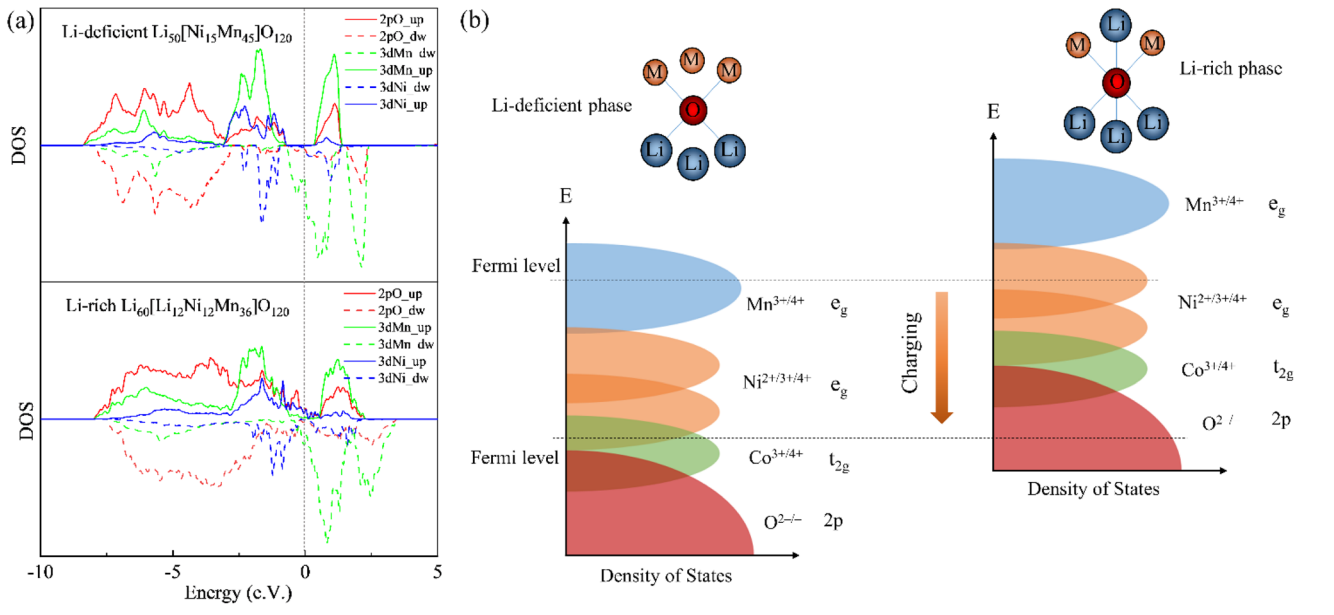

Fig. 4 (a) The projected density of states (DOS) of the O 2p orbitals and 3d TM orbitals and (b) electronic band structure of the Li-deficient phase and the Li-rich phase.

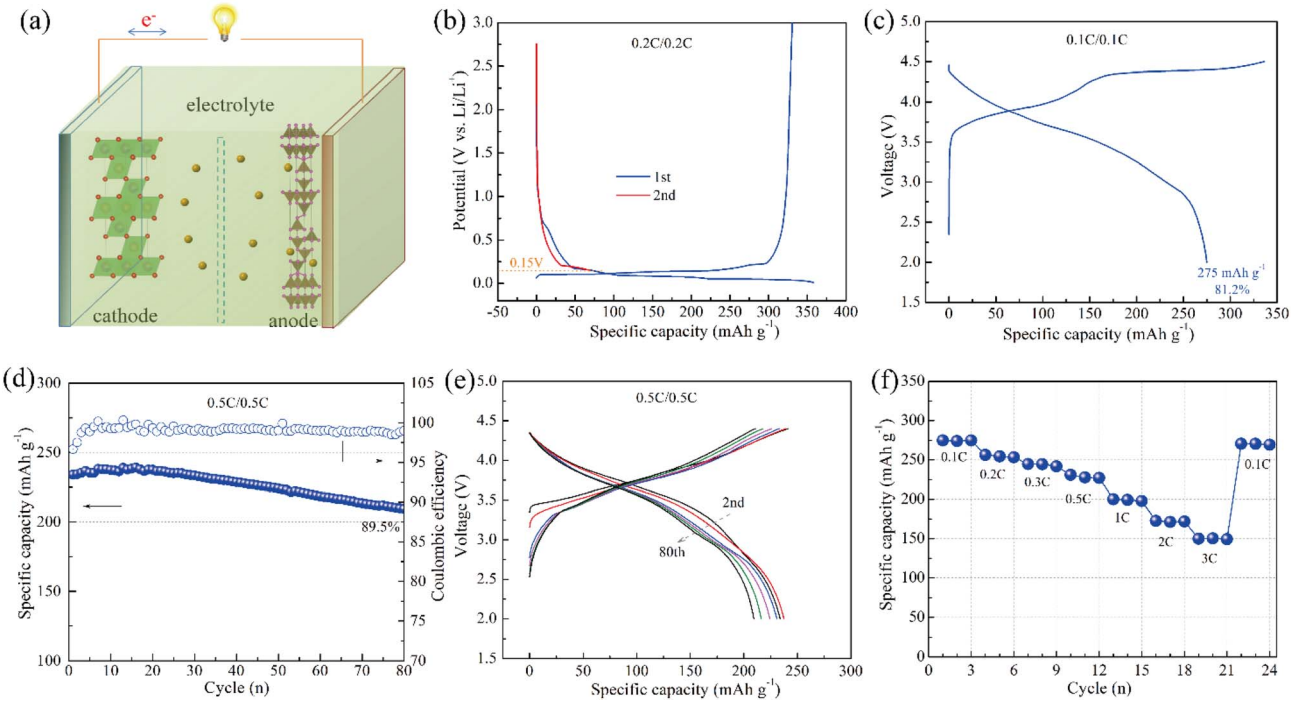

Fig. 5 (a) Scheme of the Li-ion full cells, (b) the pre-lithiated MCMB negative, (c) the first charge–discharge curves, (d) cycling stability of capacity, (e) changes of charge–discharge profiles at 0.5C, and (f) rate performance of full cells.

phase transformation from the layered structure to spinel/rock-salt structure and capacity/voltage decline, and needs to be eliminated or minimized at all costs. The L-T ion exchange causes the phase transition from the Na-deficient P3-type structure to the Li-deficient O3′-type structure. The Li-deficient phase removes TM layer cations replaced by Li ions, and then the initial TM valence would drop below +3, which restrains oxygen anion redox activity and facilitates cationic redox contribution, as depicted in Fig. 4(b). Consequently, the Li-deficient and Li-rich biphasic structure suppresses the oxygen mobility overflow on the Li-rich grain surface, and improves the oxygen-anionic redox reversibility and capacity/voltage stability.

As for the LLOs, the lattice oxygen loss occurs in the initial charging process and thereby results in structural reconstruction and a low ICE.[7] The pre-lithiated negative can compensate for the active Li loss, especially in the first charge–discharge cycle, and further improve the energy density and cycling performance of full cells. Li-ion full cells coupling the BI-LLOs positive and the pre-lithiated mesocarbon microbeads (MCMB) negative are designed, as illustrated in Fig. 5(a). The designed capacity of negative/positive is about 1.1 for full cells. The MCMB negative is first pre-lithiated and the charge–discharge curves are shown in Fig. 5(b). For simplicity, the specific capacity of full cells is calculated based on the positive mass only while the energy density is calculated according to the total mass of full cells. The full cells show a high available capacity of 275 mAh g^{-1} at 0.1C with a median discharge voltage of 3.46 V as shown in Fig. 5(c). The mass of the layered positive electrode accounts for ~35 wt% of the total mass of a pouch full cell,[51] and this assembled full cell can deliver a high energy density of ~350 Wh kg^{-1}. The full cells still possess a discharge specific capacity of 247.4 mAh g^{-1} after 80 charge–discharge cycles at 0.5C as shown in Fig. 5(d), which corresponds to a good capacity retention of ~90%. The changes in charge–discharge profiles during repeated cycles are shown in Fig. 5(e), in which the increasing charge platform and decreasing discharge platform indicate weak electrochemical polarization as the number of cycles increases.[52,53] The full cells also exhibit a good cycling stability of median voltage as shown in Fig. S14. The full cells show the available capacities of 274, 255, 243, 228, 200, 172, and 150 mAh g^{-1} at 0.1C, 0.2C, 0.3C, 0.5C, 1C, 2C to 3C, respectively, as shown in Fig. 5(f). The superior electrochemical performance confirms that the BI-LLOs show great potential for developing high-energy Li-ion full-cell systems.

3 Conclusions

In summary, Li-rich and Li-deficient biphasic intergrowth cathodes are rationally designed and prepared *via* Li/Na ion exchange from the P3/O3 intermediate mixed-phase composite. The incorporation of the Li-deficient structure makes the movement of O 2p non-bonding energy band toward lower energy, reduces the lattice oxygen loss and thus enables the reversibility of the oxygen-anionic redox chemistry, which further remarkably enhances the voltage/capacity stability of LLOs. The BI-LLOs also show a high available capacity reaching 300 mAh g^{-1} with an improved ICE of ~88%. Besides, the BI-LLOs as high-capacity cathodes show great potential for developing high-energy Li-ion full cells. These findings demonstrate

the feasibility of tuning oxygen-anionic redox chemistry and improving electrochemical properties by introducing a Li-deficient phase into a Li-rich phase.

Author contributions

Feng Li: investigation, methodology, writing – original draft, funding acquisition. Jiacheng Li: investigation, writing – original draft, formal analysis. Peiyu Hou: conceptualization, writing – review and editing, funding acquisition. Zezhou Lin: formal analysis. Mohan Dong: formal analysis. Linhui Wang: conceptualization, writing – review and editing. Hongzhou Zhang: conceptualization, writing – review and editing, funding acquisition. Xijin Xu: conceptualization, writing – review and editing.

Conflicts of interest

The authors declare no competing financial interests.

Data availability

The data supporting this article are available from the corresponding author upon reasonable request.

Supplementary information: experimental section, characterization data for precursor, P3/O3 intermediate phase, SP-LLOs and BI-LLOs. See DOI: **https://doi.org/10.1039/d5sc04623h**.

Acknowledgements

This work was funded by the National Natural Science Foundation of China (No. 22379052 and 22479112), the Taishan Scholars of Shandong Province (No. tsqn202507210 and tsqnz20221143), and the Tianjin Science & Technology Program (No. 22YFYSHZ00220).

Notes and references

1 M. Armand and J. M. Tarascon, *Nature*, 2008, **451**, 652–657.
2 W. Li, B. Song and A. Manthiram, *Chem. Soc. Rev.*, 2017, **46**, 3006–3059.
3 W. Kong, C. Zhao, S. Sun, L. Shen, X. Huang, P. Xu, Y. Lu, W. Huang, J. Huang and Q. Zhang, *Adv. Mater.*, 2024, **36**, 2310738.
4 C. Wen, E. Zhao, M. Zhang, X. Wang, E. Hu, J. Liu, X. Yu, M. Olguin, T. Wynn, Y. Meng, K. Page, F. Wang, H. Li, X. Yang, X. Huang and L. Chen, *Energy Storage Mater.*, 2020, **24**, 384–393.
5 L. Bao, L. Wei, N. Fu, J. Dong, L. Chen, Y. Su, N. Li, Y. Lu, Y. Li, S. Chen and F. Wu, *J. Energy Chem.*, 2022, **66**, 123–132.
6 Y.-S. Zhao, F.-F. Wang, J.-C. Wang, P.-F. Wang, T.-F. Yi and J.-H. Zhang, *Rare Met.*, 2024, **43**, 3647–3660.
7 M.-J. Peng, J.-Q. Zhou, T.-T. Han, Y. Zhou, J. Liu, N. Xu, Z.-K. Wang, W.-B. Lin and C.-L. Yan, *Rare Met.*, 2024, **43**, 2527–2535.
8 G. Assat and J. Tarascon, *Nat. Energy*, 2018, **3**, 373–386.
9 B. Li and D. Xia, *Adv. Mater.*, 2017, **29**, 1701054.
10 R. House, G. Rees, M. Pérez-Osorio, J. Marie, E. Boivin, A. Robertson, A. Nag, M. Garcia-Fernandez, K. Zhou and P. Bruce, *Nat. Energy*, 2020, **5**, 777–785.
11 G. Assat, D. Foix, C. Delacourt, A. Iadecola, R. Dedryvere and J. Tarascon, *Nat. Commun.*, 2017, **8**, 2219.
12 E. Hu, X. Yu, R. Lin, X. Bi, J. Lu, S. Bak, K. Nam, H. Xin, C. Jaye, D. Fischer, K. Amine and X. Yang, *Nat. Energy*, 2018, **3**, 690.
13 M. Gu, I. Belharouak, J. Zheng, H. Wu, J. Xiao, A. Genc, K. Amine, S. Thevuthasan, D. Baer, J. Zhang, N. Browning, J. Liu and C. Wang, *ACS Nano*, 2013, **7**, 760–767.
14 B. Xu, C. Fell, M. Chi and Y. Meng, *Energy Environ. Sci.*, 2011, **4**, 2223–2233.
15 X. Gou, Z. Hao, Z. Hao, G. Yang, Z. Yang, X. Zhang, Z. Yan, Q. Zhao and J. Chen, *Adv. Funct. Mater.*, 2022, **32**, 2112088.
16 X. Zhang, J. Shi, J. Liang, Y. Yin, J. Zhang, X. Yu and Y. Guo, *Adv. Mater.*, 2018, **30**, 1801751.
17 J. Meng, L. Xu, Q. Ma, M. Yang, Y. Fang, G. Wan, R. Li, J. Yuan, X. Zhang, H. Yu, L. Liu and T. Liu, *Adv. Funct. Mater.*, 2022, **32**, 2113013.
18 J. Zhang, F. Cheng, S. Chou, J. Wang, L. Gu, H. Wang, H. Yoshikawa, Y. Lu and J. Chen, *Adv. Mater.*, 2019, **31**, 1901808.
19 Y. Zuo, B. Li, N. Jiang, W. Chu, H. Zhang, R. Zou and D. Xia, *Adv. Mater.*, 2018, **30**, 1707255.
20 C. Cui, X. Fan, X. Zhou, J. Chen, Q. Wang, L. Ma, C. Yang, E. Hu, X. Yang and C. Wang, *J. Am. Chem. Soc.*, 2020, **142**, 8918–8927.
21 D. Eum, B. Kim, S. Kim, H. Park, J. Wu, S. Cho, G. Yoon, M. Lee, S. Jung, W. Yang, W. Seong, K. Ku, O. Tamwattana, S. Park, I. Hwang and K. Kang, *Nat. Mater.*, 2020, **19**, 419–427.
22 X. Cao, H. Li, Y. Qiao, M. Jia, X. Li, J. Cabana and H. Zhou, *Adv. Mater.*, 2021, **33**, 2004280.
23 P. Liu, H. Zhang, W. He, T. Xiong, Y. Cheng, Q. Xie, Y. Ma, H. Zheng, L. Wang, Z. Zhu, Y. Peng, L. Mai and D. Peng, *J. Am. Chem. Soc.*, 2019, **141**, 10876–10882.
24 X. Jia, Z. Jian, H. Liu, L. Kong, Z. Li, H. Dong, M. Zhang, L. Qiu, J. Wang, S. Chen, X. Wu, X. Guo and Y. Xiao, *Chem. Sci.*, 2024, **15**, 5192.
25 P. Hou, M. Dong, F. Li, Z. Lin and X. Xu, *Adv. Funct. Mater.*, 2024, **34**, 2409518.
26 P. Hou, M. Gong, M. Dong, Z. Lin, J. Huang, H. Zhang and F. Li, *Energy Storage Mater.*, 2024, **72**, 103750.
27 G. Zhang, X. Wen, Y. Gao, R. Zhang and Y. Huang, *Nano-Micro Lett.*, 2024, **16**, 260.
28 J. Feng, Y. Jiang, F. Yu, W. Ke, L. Que, J. Duh and Z. Wang, *J. Energy Chem.*, 2022, **66**, 666–675.
29 Y. Chen, Y. Liu, J. Zhang, H. Zhu, Y. Ren, W. Wang, Q. Zhang, Y. Zhang, Q. Yuan, G. Chen, L. Gallington, K. Li, X. Liu, J. Wu, Q. Liu and Y. Chen, *Energy Storage Mater.*, 2022, **51**, 756–763.
30 F. Li, J. Li, M. Gong, Z. Lin, X. Chang, M. Dong and P. Hou, *Rare Met.*, 2025, **44**, 2945–2957.
31 V. Hebbar, M. Viji, S. Ghosh and C. Sudakar, *Mater. Res. Bull.*, 2024, **180**, 113057.

32 W. Yu, L. Zhao, Y. Wang, C. Yang, J. Wang, H. Huang, A. Wu, X. Dong and G. Cao, *J. Colloid Interface Sci.*, 2023, **648**, 820–833.
33 G. Zhang, M. Chen, C. Li, B. Wu, J. Chen, W. Xiang, X. Wen, D. Zhang, G. Cao and W. Li, *Chem. Eng. J.*, 2022, **443**, 136434.
34 Y. Chen, G. Li, Z. Xie, P. Huang, X. Li, F. Li and W. Yan, *Energy Fuels*, 2023, **37**, 6800–6809.
35 Y. Zhang, X. Shi, S. Zheng, Y. Ouyang, M. Li, C. Meng, Y. Yu and Z. Wu, *Energy Environ. Sci.*, 2023, **16**, 5043–5051.
36 D. Fu, X. Zhang, Y. Zhou, K. Yang, J. Fan, L. Li and C. Fu, *ACS Sustainable Chem. Eng.*, 2025, **13**, 3311–3320.
37 J. Mei, G. Gao, Y. Chen, W. Xu, W. He, S. Li, Q. Xie, L. Wang, P. Liu, Z. Zhu and D. Peng, *ACS Sustainable Chem. Eng.*, 2024, **12**, 1353–1364.
38 X. Han, A. Liu, S. Wang, Y. Liu, S. Li, Y. Zhang, H. Zheng, B. Sa, L. Wang, J. Lin, B. Qu, Q. Xie and D. Peng, *Small*, 2023, **19**, 2303256.
39 T. Li, Y. Xiao, T. Zhu, Y. Li and W. Wang, *Small Methods*, 2025, **9**, 2401206.
40 X. Tao, Z. Zheng, Z. Ma, H. Yu, T. Hui and F. Bei, *ACS Appl. Mater. Interfaces*, 2024, **16**, 36774–36783.
41 L. Wu, Z. Li, J. Chen, Y. Zhang, R. Wang, S. Cao, H. Ding, M. Liu, H. Liu and X. Wang, *ACS Appl. Mater. Interfaces*, 2024, **16**, 34880–34891.
42 S. Yuan, J. Guo, Y. Ma, Y. Zhou, H. Zhang, D. Song, X. Shi and L. Zhang, *ACS Appl. Energy Mater.*, 2021, **4**, 11014–11025.
43 A. Armstrong, M. Holzapfel, P. Novák, C. Johnson, S. Kang, M. Thackeray and P. Bruce, *J. Am. Chem. Soc.*, 2006, **128**, 8694–8698.
44 Z. Lin, Y. Ying, Z. Xu, G. Chen, X. Gong, Z. Wang, D. Guan, L. Zhao, M. Yang, K. Fan, T. Liu, H. Li, H. Zhang, H. Li, X. Zhang, Y. Zhu, Z. Lu, Z. Shao, P. Hou and H. Huang, *Energy Environ. Sci.*, 2025, **18**, 334–346.
45 Z. Lin, K. Fan, T. Liu, Z. Xu, G. Chen, H. Zhang, H. Li, X. Guo, X. Zhang, Y. Zhu, P. Hou and H. Huang, *Nano-Micro Lett.*, 2024, **16**, 48.
46 S. Ramakrishnan, B. Park, J. Wu, W. Yang and B. McCloskey, *J. Am. Chem. Soc.*, 2020, **142**, 8522–8531.
47 P. Hou, F. Li, H. Zhang and H. Huang, *J. Mater. Chem. A*, 2020, **8**, 14214–14222.
48 F. Li, Y. Lin, J. Liu, J. Chen, X. Wan, L. Zhao, L. Xi, Z. Li, H. Zhang, X. Xu, Z. Zhou, B. Su, M. Zhu and J. Liu, *Energy Environ. Sci.*, 2025, **18**, 1241–1254.
49 J. Hong, W. Gent, P. Xiao, K. Lim, D. Seo, J. Wu, P. Csernica, C. Takacs, D. Nordlund, C. Sun, K. Stone, D. Passarello, W. Yang, D. Prendergast, G. Ceder, M. Toney and W. Chueh, *Nat. Mater.*, 2019, **18**, 256–265.
50 G. Sun, F. Yu, L. Que, L. Deng, M. Wang, Y. Jiang, G. Shao and Z. Wang, *Nano Energy*, 2019, **66**, 104102.
51 J. Lee, C. Yoon, J. Hwang, S. Kim, F. Maglia, P. Lamp, S. Myung and Y. Sun, *Energy Environ. Sci.*, 2016, **9**, 2152–2158.
52 C. Sun, B. Zhao, Q. Wen, X. Chen, N. Hong, J. Zeng, J. Zhang, L. Li, J. Wang, X. Zhang and J. Zheng, *Chem. Sci.*, 2025, **16**, 4842.
53 L. Chen, C. Chiang, X. Wu, Y. Tang, G. Zeng, S. Zhou, B. Zhang, H. Zhang, Y. Yan, T. Liu, H. Liao, X. Kuai, Y. Lin, Y. Qiao and S. Sun, *Chem. Sci.*, 2023, **14**, 2183.